PHYSICAL SCIENCES

Fluid dynamical pathways of airborne transmission while waiting in a line

Ruixi Lou[1,2], Milo Van Mooy[1], Gabriel A. Tarditti[3], Rodolfo Ostilla Monico[3], Varghese Mathai[1,4]*

Waiting in a line (or a queue) is an unavoidable social interaction that occurs frequently in public spaces. Despite its wide prevalence and rich parametric variability, few studies have addressed the risks of airborne infection while waiting in a line. Here, we use a combination of laboratory experiments and direct numerical simulations to assess the flow patterns in a simplified waiting line setting. From observations of the transport of breath-like expulsions, we reveal the presence of fluid dynamical counter-currents —due to the competing effects of line kinematics and thermal gradients. Depending on the walking speed, an intermediate temperature range can potentially heighten the infection risks by allowing the breath plume to linger; however, colder and warmer ambients both suppress the spread. Current guidelines of increasing physical separation appear to have a limited impact on reducing aerosol transmission. This work highlights the need for updated transmission mitigation guidelines in settings where physical separation, interaction duration, and periodicity of movements are factors.

INTRODUCTION

The COVID-19 pandemic has redefined the ways in which we interact in social settings. From social distancing and mask wearing to testing and contact tracing, these measures have proven to be effective in mitigating the ever-present risks of infections. It has now been recognized that a variety of respiratory pathogens, including Rous sarcoma virus, severe acute respiratory syndrome coronavirus 2, and influenza are spread primarily through tiny droplets and airborne particles released by asymptomatic and presymptomatic individuals during speaking and breathing (*1*). These respiratory contaminants are typically less than 10 μm in size (*2*, *3*), which can enable them to remain suspended in the air for minutes to several hours depending on the ambient conditions (*4*–*6*). Although physical distancing and the wearing of face masks are common measures used to reduce the spread of infections (*7*–*16*), these provide little insight into the transport of aerosols in situations where the duration of interactions and the time history of the movements of individuals become a factor. The problem is further intensified under varying influences of thermal gradients and buoyancy-driven plumes in indoor spaces, which can vary substantially across climate zones and biomes (*4*, *5*, *17*–*31*).

Almost all of the studies of airborne transmission take the perspective of infections occurring under "static" interaction conditions, such as across desks in a classroom setting or individuals interacting in a face-to-face meeting standing or while seated in a passenger car next to an infected individual (*2*, *32*). Consequently, current guidelines for transmission mitigation are based almost entirely on static, physical distancing–based recommendations—such as the "six-feet" rule and reducing the duration of interactions. In contrast, a wide class of social interactions occur in our daily lives that are distinctly outside the domain of static interactions. A familiar example is that of waiting and walking in a line—at a grocery store or a vaccination clinic or an airport security. The indoor waiting line introduces considerable complexity to the modeling of aerosol transmission due to the additional time and length scales of periodic walking and stopping, the physical separation (guided or self-imposed), and the variations in ambient temperature. In particular, currents generated by the movement of people interact with the aerosols, advecting, and diffusing while also being convected (upward or downward) by the thermal gradient effects with the ambient (*6*, *33*–*35*) can lead to complicated pathways of infection. Despite the ubiquity of these interactions, few studies have addressed airborne cross-infection risks in a waiting line (queue).

Here, we study the simplified case of periodically walking and halting individuals in a waiting line, by using a combination of laboratory experiments and direct numerical simulations (DNS), focusing on the large-scale transport of aerosols released during regular breathing of the individuals in the line. The movements of people in the waiting area can be separated into two stages: a waiting period, followed by a brief walking period (Fig. 1A). We ask the question: Where do the aerosols released by an infectious individual in a waiting line end up (denoted by the yellow cloud in Fig. 1A)? During the waiting phase, we assume that an infectious person continually releases (breathes) airborne particles around them which slowly diffuse into the surrounding air. After some time elapses, they walk to the next position in line. The resulting reorganization of individuals advects and diffuses the airborne particles. Except in very slow situations, the diffusion may be considered subdominant (Fig. 1B), with the characteristic diffusion timescale τ_d much larger than the average waiting period τ_l. Two distinct processes may disperse the virus-laden aerosols: (i) the flows (air currents) induced by walking humans and (ii) the buoyancy (thermally driven) of breath plumes. For a variety of waiting line scenarios, the timescales of walking and buoyancy can be comparable, and a complex, coupled interplay between the two can be expected. We will reveal how the competition between shear (line kinematics) and buoyancy (thermal gradients) (*36*, *37*) can emerge as an important criterion for transmission risks in the waiting line.

A number of practical challenges exist to conducting field experiments with human subjects in a waiting line while also varying the physical parameters in the problem. Hence, we apply the concept of dynamic similarity to transform the waiting line to a laboratory setting with a controlled, driven conveyor belt system of three-dimensional

[1]Department of Physics, University of Massachusetts, Amherst, MA 01003, USA. [2]Department of Physics, University of Chicago, Chicago, IL 60637, USA. [3]School of Engineering, University of Cadiz, Cádiz, Andalusia 11001, Spain. [4]Department of Mechanical and Industrial Engineering, University of Massachusetts, Amherst, MA 01003, USA.
*Corresponding author. Email: vmathai@umass.edu

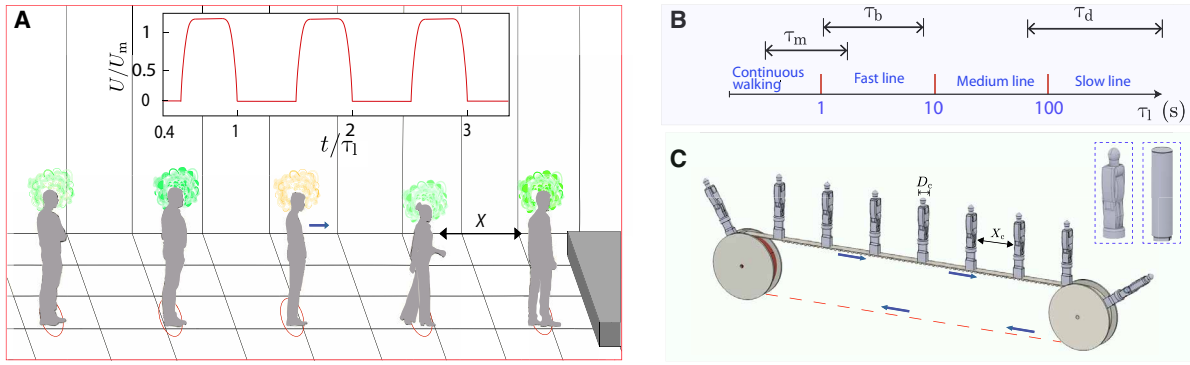

Fig. 1. Schematic representations of airborne transmission while waiting in a line. (**A**) A simplified schematic representation of people waiting and walking in a line. The green clouds represent the "breath plumes" of individuals, while the yellow cloud represents the breath plume released by a potentially infectious (asymptomatic) individual in the waiting line. The inset shows an example of the velocity, which is marked by periodic start-stop cycles, where $U(t)$ is the instantaneous velocity, U_m is the walking speed, and τ_l is the time period of the line. (**B**) Comparison of the moving timescale τ_m with the characteristic timescales of diffusion τ_d and buoyancy τ_b. We can classify the line movement as fast/medium/slow depending on the time period τ_l of the waiting line movement. (**C**) A pulley-driven conveyor belt system carrying equally spaced 3D printed human-shaped dummies on a belt. Inset shows schematics of a human-shaped model and a simplified, cylindrical model, both of which were tested.

(3D) printed dummies [Fig. 1C and see the Supplementary Materials]. In combination with the experiments, fully resolved DNS were used to gain further insights into the emergent flow patterns and the Lagrangian trajectories of the tracer particles. The periodic movements may be reduced into a set of nondimensional parameters that characterize the flow: a Reynolds number, a Grashof number, a reduced frequency, and a dimensionless spacing. The Reynolds number is defined as $Re = UD_s/\nu$, where D_s and U are the characteristic length and velocity scales, respectively, and ν is the kinematic viscosity of the fluid. For the waiting line, the relevant characteristic length is D_s, the shoulder width of a person, and U is a characteristic walking speed, taken as the walking speed U_m. While the average unimpeded walking speed of humans is around 3.3 mph (~1.5 m/s), typically in indoor spaces and under recurrent start-stop conditions (such as in a waiting line), the peak walking speed may lie in the range of 0.5 to 0.87 m/s (*38*). Consequently, for the typical waiting line, Re can lie in the range of $[1 \text{ to } 1.8] \times 10^4$, indicating turbulent flow. For this range of Re, a nearly Reynolds-independent large-scale flow can be expected, and therefore, the shear buoyancy competition dominates over any enhanced spreading/dilution of aerosols due to turbulent mixing. The strength of buoyancy effects coming from breath plumes is quantified through the Grashof number, $\mathrm{Gr} = g\beta\Delta T D_s^3/\nu^2 = U_b^2 D_s^2/\nu^2$, where g is the gravitational acceleration, β is the thermal expansion coefficient of the fluid, ΔT is the temperature difference between human exhalation and the ambient background, and $U_b = \sqrt{g\beta\Delta T D_s}$ is the characteristic free-fall (buoyancy) velocity. We may note that a typical temperature difference of $\Delta T = 4°\mathrm{C}$ corresponds to $\mathrm{Gr} \approx 2.5 \times 10^7$. In addition, we define the velocity ratio $\hat{U} = U_b/U_m = \sqrt{\mathrm{Gr}}/Re$ as a way of measuring the strength of buoyancy compared to advection. The two other nondimensional parameters in the system are the nondimensional separation, defined as $A^* = X/D_s$, where X is the separation between people in the waiting line, and the nondimensional frequency of motion, defined as $f^* = \tau_m/\tau_l$, where $\tau_m = X/U_m$ is the moving time and τ_l is the total period composed of moving and waiting times during a cycle of motion (i.e., the time between starting to move from one spot to a new spot and again starting to move from that spot).

RESULTS AND DISCUSSION

In the present study, we limit $A^* = 5$ (equivalent to six-foot separation) and $f^* = 0.17$, i.e., a waiting time that is five times longer than the walking time. We varied $A^* \in [2.5-10]$ and f^* covering the range of medium to slow lines (Fig. 1 from $\tau_l \sim 10$ to 100 s), and it was seen that physical separation, unexpectedly, has only a minor effect on aerosol spreading (see the Supplementary Materials and fig. S2). The risk of cross-infection was highest for the nearby individuals in the line, as there was not sufficient time for the released airborne particles to disperse. Thus, the transport from the infected individual to the trailing susceptible individual will be our focus in the present work.

Experiments

We rely on a basic model of a waiting line composed of equally spaced 3D printed models, as shown in the schematic of Fig. 1C. Both 3D printed human-shaped models and cylindrical models of matched equivalent diameter were tested in a laboratory-scale, driven conveyor belt system. The rationale behind testing both shapes was to assess whether the primary flow features were similar under a simplification of the geometry of the model. The belt was driven by a stepper motor and controlled using an Arduino microcontroller. Since the kinematic viscosity ν of water is nearly one order of magnitude lower than that of air, we can scale down the physical size of the experiment while also ensuring geometric, kinematic, and dynamic similarity of the physical system (*39*). For the in-laboratory conditions, the scaled height and width of the average person were 110 and 25 mm, respectively, and the recommended 2 m (≈6 ft) separation between individuals was scaled down to 125 mm. The walking time, the walking speed, and the waiting time were precisely controlled using a stepper motor driving the conveyor belt system [Fig. 1C and the Supplementary Materials]. All physical variables were scaled down (or up) to match the relevant dimensionless numbers. During the experiments, we used ultraviolet-induced fluorescence (see Fig. 2), combined with time-resolved particle imaging velocimetry (PIV) to visualize the passive/active scalar transport and the underlying fluid motion. As shown in Fig. 2 (A to C) (top

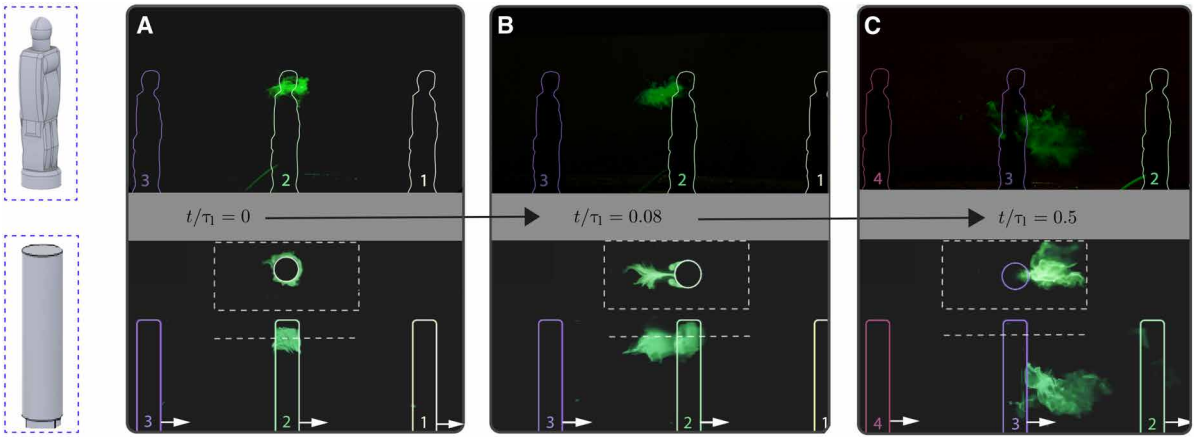

Fig. 2. Experimental visualization of the transport of released dye in a laboratory-scale realization of a waiting line. (**A**) Distribution of the dye at time $t / \tau_l = 0$, corresponding to the moment the models begin to move, for human-shaped models (top row) and cylindrical models (bottom row). Here, 1 to 3 represent the different models, and their relative locations at later times ($t / \tau_l = 0.08$ and $t / \tau_l = 0.5$) are shown in (B) and (C). (**B**) Spread of the dye at the intermediate time, $t / \tau_l = 0.08$, during the walking cycle when the cylinders are moving. (**C**) Location of the dye at $t / \tau_l = 0.5$. For both human-shaped models and cylindrical models, the dye is observed to be pushed downward in (C), which provides an indication of an underlying flow pattern (downwash).

and bottom rows), the transport patterns of the two cases (human-shaped models and cylindrical models) are comparable—with a strong downwash transporting the plume downward. Experiments at different levels of plume buoyancy also showed similar transport for human-shaped and cylindrical models (see the Supplementary Materials). The kinematically driven large-scale flow patterns are expected to be captured even under the simplification of a cylindrical bluff body of the same equivalent diameter. Hence, PIV measurements may be performed on cylindrical models (discussed later in Fig. 3) as it is simpler to refractive index–match them, compared to the human-shaped models.

To match buoyancy effects, the temperature-density equivalence, applicable for small thermal gradients, was used in the experiments. The temperature-density correspondence, when transforming from a waiting line in the air to a laboratory setting is

$$\Delta\Gamma = \left(\frac{D_s}{D_c}\right)^3 \left(\frac{\nu}{\nu_a}\right)^2 \beta \Delta T \tag{1}$$

where $\Delta\Gamma$ is the proportional density increase, $\Delta\Gamma = \Delta\rho / \rho$, where ν and ν_a are the kinematic viscosities of the fluid and that of air, respectively, and D_c is the cylinder diameter. For reference, $\Delta\Gamma = 0.16$ in our experiment would correspond to a temperature difference of about 4°C between breath and ambient, following a model for exhaled breath temperature as a function of ambient temperature and skin temperature (*4*, *40*, *41*).

Numerical simulations

DNS were used to further validate the experimental observations and to gain deeper insights into particle transport. We simulated the (nondimensional) incompressible Navier-Stokes equations

$$\frac{\partial \mathbf{u}}{\partial t} + \mathbf{u} \cdot \nabla \mathbf{u} = -\nabla p + \frac{1}{Re} \nabla^2 \mathbf{u} + \mathbf{f}_b + \mathbf{f}_i \tag{2}$$

in a straight parallelepiped domain, where $\mathbf{u}$ is the nondimensional fluid velocity, p is the pressure, and t is the time. Two body forces appear, a buoyancy force $\mathbf{f}_b$ to model thermal effects under the Boussinesq approximation, and an immersed boundary force $\mathbf{f}_i$, which incorporates the forcing on the fluid due to the movements of the cylinders (*42*). We used the open-source code AFiD (*43*), which has been widely used to simulate fluid dynamic problems. The code uses a centered, energy-conserving finite differences in space and a third-order Runge-Kutta fractional time-stepping.

The moving cylinders are maintained to have a similar height-to-diameter ratio as in the experiments, and the Reynolds number was set to $Re = 6000$. This value of Re, although lower than in the experiment, is sufficiently large that the flow patterns are nearly Reynolds independent (shown later in Fig. 3). The boundary condition on the cylinder body was set as a constant temperature. Taking 37°C as the human core temperature, the human periphery temperature changes in relation to the ambient temperature (*41*). The breath plume was released at a fixed initial temperature according to the breath-temperature relation in (*40*, *41*) (see also the Supplementary Materials). In addition, a fixed scalar was assigned to the plume, a proxy for the concentration of infectious particles, and the two scalars were allowed to evolve in time. To account for the buoyancy change due to varying ambient temperature range of 24° to 35°C, Gr was varied in the range of $[0 \text{ to } 2.5] \times 10^7$. Here, $\mathrm{Gr} = 0$ ($\widehat{U} = 0$) corresponds to the condition with zero thermal gradients (an idealization), and $\mathrm{Gr} = 2.5 \times 10^7$ ($\widehat{U} = 0.83$) corresponds to a temperature difference between breath and ambient of $\Delta T \approx 4$°C following (*40*, *41*).

The spreading of airborne particles (dye) is studied using a standard advection-diffusion equation for a scalar C (*44*, *45*)

$$\frac{\partial C}{\partial t} + \mathbf{u} \cdot \nabla C = \mathrm{Sc}^{-1} Re^{-1} \nabla^2 C + \phi_C \tag{3}$$

The scalar C can be taken as as either a temperature field or as a dye concentration, with a Schmidt number $\mathrm{Sc} = D / \nu$, and with D the diffusion coefficient of the scalar. We set the scalar diffusivity to be equal to the fluid kinematic viscosity. This reduces resolution requirements while reproducing the main features of the flow that the scalar can reveal (*45*, *46*). For the small to moderate temperature

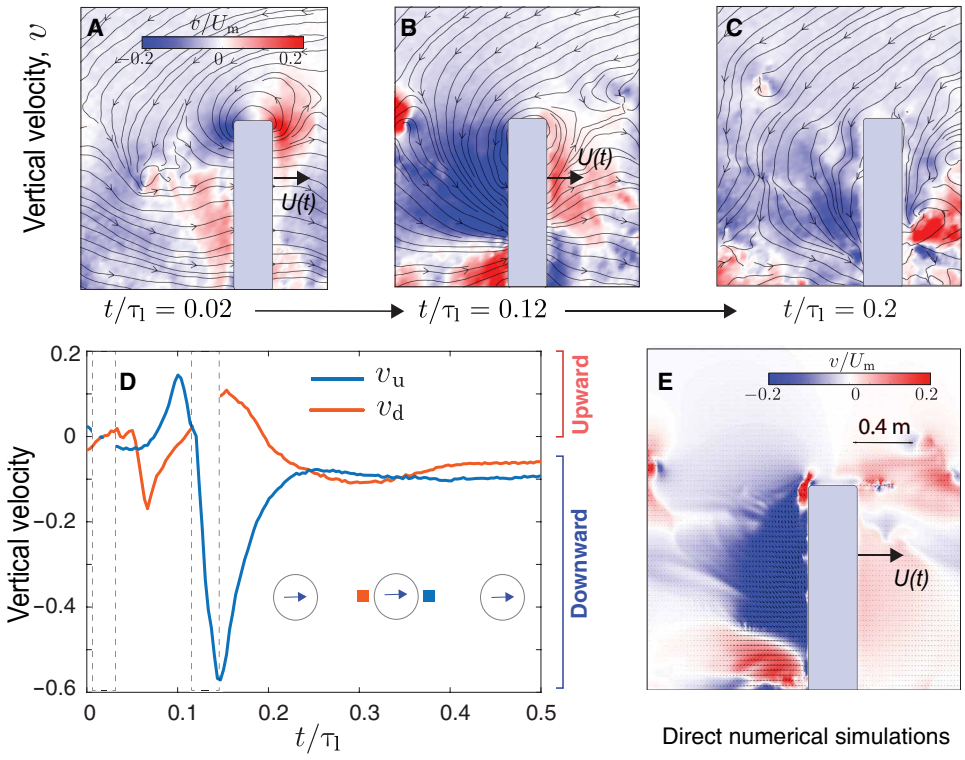

Fig. 3. Experiments and DNS of the velocity fields generated by periodic movements in the waiting line. (**A** to **C**) Vertical velocity fields obtained from PIV with streamlines showing the strong downwash generated soon after the cylinders are in motion. Normalized vertical velocity at the blue and red marked locations in front of and behind the cylinder are shown in (**D**). The blanked intervals in (D) correspond to the crossing of the cylinder. (**E**) Vertical velocity field obtained from DNS, at $t/\tau_l = 0.12$.

differences, common in natural convection, thermal effects scale linearly as a buoyancy force, $\mathbf{f}_b$ (*47*); in Eq. 2, $\mathbf{f}_b = \widehat{U}\,\mathrm{Ce}_y$, where $\widehat{U}$ was defined above as $\widehat{U} = U_b/U_m$.

For the particle concentration analysis, a spatial resolution of 256 × 384 × 768 was used, with clustering of points in the y direction close to the bottom wall. The flow was initialized for zero velocity, and the cylinders were moved for four start-stop cycles. After this, the dye field is initialized to zero everywhere, except for a spatial region around the "infected" cylinder, mimicking the dye release in the experiment (Fig. 2A). In addition, 1000 Lagrangian tracer particles distributed were released from this region. We simulated the system for four more cycles, collecting velocities, scalar fields, and particle trajectories.

We first consider the buoyancy-less case ($\widehat{U} = 0$) with an experiment where a passive, fluorescent dye is released from one of the cylinders, #2 (the infectious) as shown in Fig. 2. The dye can be considered as a proxy for aerosols released by an infectious individual during breathing, and by observing its evolution in time, we can analyze where the infectious aerosols get transported to after one cycle of walking and waiting. The top view and side view recordings are shown in Fig. 2 (A to C) and insets, corresponding to $t/\tau_l = 0$, 0.08, and 0.5, respectively. The visualization indicates that the released particles concentrate in front of the trailing (susceptible) person with not much dilution (as suggested by the intensity of the dye in the top view of Fig. 2C). Despite the dye being nearly perfectly density matched with the fluid, it still sinks in front of the susceptible walker (#3 cylinder) soon after the walking phase ends.

To understand the origin of the downward drift of the dye, we study the underlying flow field using both time-resolved PIV experiments and DNS. Figure 3 (A to C) shows the vertical velocity and the flow streamlines at successive points of the movement. A strong, circulating flow is created initially ($t/\tau_l = 0.02$), which traps the aerosols at their release location, although the individuals in the line move forward (see also inset to Fig. 2B). However, this is immediately followed by a sudden downwash current (blue regions in Fig. 3B at $t/\tau_l = 0.02$). This downwash current is responsible for the downward drift of the dye (observed earlier in Fig. 2) and is reminiscent of the wake with a "starting vortex" generated behind an airplane wing or that behind a circulation-generating bluff body undergoing a start-stop motion (*48*). To quantify the strength of the downwash, in Fig. 3D, we sample the vertical velocity at fixed points in space while the walkers (cylinders) move past these points. A strong downward current is formed downstream of the walker, which peaks in strength ($v \approx -0.6U_m$) around $t \approx 0.15\tau_l$. By $t \approx 0.25\tau_l$, the downdraft velocity has reduced in strength, to about 10% of the walking speed, but the downdraft persists at this value for the remainder of the waiting period. From a purely kinematic viewpoint, therefore, a sinking of the infectious plume can be expected (as seen in Fig. 2), which presumably reduces the infection risk for the trailing individuals in the waiting line.

We compare the velocity fields from DNS with those measured from PIV (Fig. 3, B and E) at $t/\tau_l = 0.12$. Despite the difference in Reynolds number in the experiment and DNS, nearly the same large-scale flow features are observed, including the strong downwash. Furthermore, the normalized velocities are remarkably similar

in magnitude. These further ascertain the assumption of nearly Reynolds-independent flow fields within the *Re* range in our study ([0.5 to 1.8] × 10^4). Drawing from these insights, we model the sinking speed of the breath plume as $\gamma\ U_m$, where the prefactor $\gamma \sim 0.1$ was experimentally (or numerically) confirmed.

Because thermal gradients are often present in waiting lines, the downwash will be opposed by the buoyancy of the breathed air, complicating the above picture and modifying the ultimate location of the infectious plume. We systematically vary $\hat{U}$ and study the location where the particles end up after one time period of line movement. The particle displays a remarkable sensitivity on the ambient condition, as visualized using colored dye in Fig. 4 (A to C) for ambient temperatures equivalent to 35°, 28°, and 22°C, respectively. While in the absence of buoyancy (Fig. 4A), the released dye ends up at the base of the cylinders, and for high buoyancy (Fig. 4C), the dye ends up above the cylinders. In between, at an intermediate buoyancy (Fig. 4B) the particles remain in front of the face of the (susceptible) trailing walker, indicating a high cross-infection risk. This effect is highlighted when looking at the vertical velocity of the case at 28° and 22°C in Fig. 4 (D and E): Aside from a good qualitative comparison between experiment and simulation, we can see how in both cases the infected plume has sufficient buoyancy to oppose the ever-present downwash current from the wake effects in the waiting line. In a more general context, the condition of the highest infection risk would depend crucially on the competition between line kinematics (walking speed) and the ambient temperature (buoyancy).

The increased infection risk arising from this upward current can be analyzed through a quantitative model that captures the combined effects of the counter-currents on the spread of infectious aerosols. The cloud of aerosols may be expected to rise at a velocity scale (*49*), $\sim \sqrt{g\beta\Delta T}$ which is counteracted by the downwash velocity of γU_m. Here, β is the thermal expansivity of the fluid, and $\gamma \approx 0.1$ was obtained previously (see the Supplementary Materials for further details). The resulting vertical drift after one cycle of line movement can be written as

$$Y - Y_0 = \left(\kappa\sqrt{\beta\Delta T} - \gamma\ U_m\right)\tau_l \tag{4}$$

where $\kappa \sim \sqrt{g\,\ell_p}$ and ℓ_p is the size scale of the released plume.

Figure 4F shows the model predictions for the vertical drift of the infectious plume for different ambient temperatures and walking speeds. The model shows good agreement with the vertical position of the plume obtained from the simulations (blue symbols). In addition, we can observe that the highest infection risks occur for an intermediate temperature range. The downward current (second term in Eq. 4) grows linearly with the walking speed, U_m. As discussed earlier, the typical walking speed in impeded indoor spaces could vary in the range of [0.5 to 0.87] m/s. Thus, for a slightly faster walking speed (given by the green and red curves in Fig. 4F), the downwash current would gain in intensity. We extend the model to the higher walking speeds (green curve at 1.5× and red curve

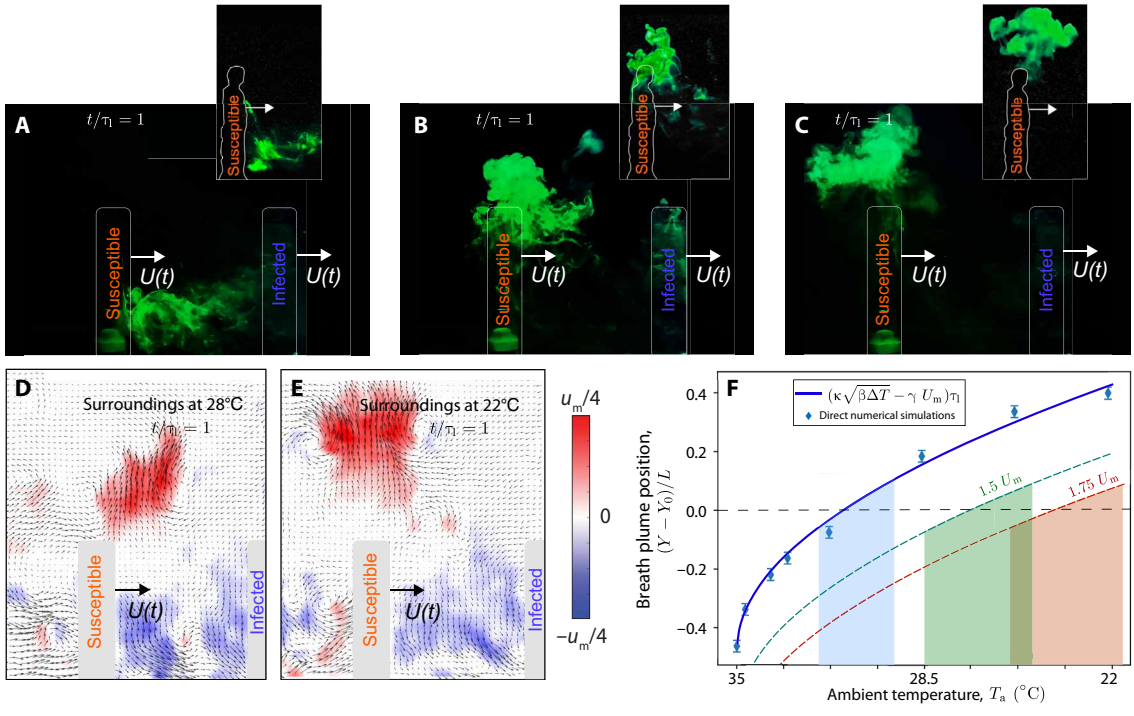

Fig. 4. Counteracting roles of line kinematics and plume buoyancy on the spread of airborne particles. (**A** to **C**) Visualization snapshot of the location of a colored dye (a proxy for infectious aerosols), originally released from the cylinder on the right side, for a relatively high ambient temperature condition, after one waiting time period, $t / \tau_l = 1$. This case is equivalent to an ambient temperature $T_a \approx 35$°C. Cases (A) to (C) show how the same kind of particles end up at different locations under the competing effects of the downwash and the breath plume's buoyancy under different ambient equivalent temperatures [$T_a \approx 35$°, 28°, and 22°C in (A), (B), and (C), respectively]. The insets in (A) to (C) show the corresponding location of the colored-dye for human-shaped models at the three ambient conditions, which suggests similar transport patterns. (**D** and **E**) Vertical velocity PIV fields show the buoyancy plume at the ambient conditions of (B) and (C), respectively. The mean vertical position of the breathing plume after one period ($t = \tau_l$) versus ambient temperature is shown in (**F**), along with the predictions of a competing flow model (blue curve).

at 1.75×). In summary, a broad range of intermediate ambient temperatures—within the human comfort temperature range—could potentially heighten the infection risks in indoor waiting lines. In contrast, our analyses show that colder and warmer ambients both suppress the risks.

Using the data from the simulations, we analyze the dispersion of particles released around the cylinder during the walking-waiting cycle. In the general situation, droplet size is an important factor in Lagrangian models as large inertial droplets can be influenced by their delayed response to the turbulent fluctuations, as well as gravitational settling, and spatial filtering effects (*50*). The Lagrangian transport equation (nondimensional) for an inertial droplet in a flow can be written as

$$\ddot{\mathbf{x}}_d = \beta \frac{D\mathbf{u}}{Dt} + \frac{1}{St}\left(\mathbf{u} - \dot{\mathbf{x}}_d\right) + \frac{1}{Fr}\hat{\mathbf{e}}_z \quad (5)$$

where $\mathbf{x}_d$ is the position of the droplet, $St = \tau_d / \tau_l$ is the Stokes number, $\beta = 3\rho_a/(\rho_a + 2\rho_d)$ is the density ratio of the droplet to air, and Fr^{-1} signifies the relative strength of gravity to inertia (*51*).

While the Lagrangian transport model is applicable for droplets of various sizes (inertia) and gravitational settling speeds, the focus of the present study is on the transmission due to individuals breathing normally (nonlabored). Prolonged exposure to asymptomatic individuals can still lead to a high load of infectious particles due to extended durations of interaction, over several wait-walk cycles. The droplet sizes released by individuals in the case of normal breathing lie in the range of 0.5 of 5 μm (*52*–*55*). In this size range, the aerosols are nearly tracers of the air flow, and their Stokesian settling speeds are very low compared to the air flow speeds (*51*). For instance, a 5-μm droplet has St ∼ 0.001 and Fr ≫ 1 since their settling velocity, $\boldsymbol{v}_s \ll \mathbf{u}$. This necessitates the condition that $\dot{\mathbf{x}}_d \approx \mathbf{u}$, i.e., the droplets nearly follow the turbulent air flow patterns (*56*).

In Fig. 5 (A and B), we show how the trajectory of particles for two cases at $T_a = 35°$ and 28°C. The particle transport behavior depends crucially on the ambient temperature: A relatively small change in T_a (~4°C) results in significantly different particle trajectories ($\hat{U}$ varies from 0 to 0.59). The effect is quantified in Fig. 5C, which shows the mean vertical displacement for the same two ambient temperature cases presented in Fig. 5 (A and B). Whether the particles end up near the zero line or not depends on both the walking speed and the temperature gradient. Next, we show the mean squared displacement (MSD) in the horizontal direction (Fig. 5) for ambient temperatures T_a in the range of 22° to 35°C, resulting in a *Gr* variation of [0 to 2.5] × 10^7. Note that the time axis is normalized with the period of line movements ($\tilde{t} = t/\tau_l$). Despite the large variation in *Gr*, the scaling and transition times of the MSDs are not affected significantly. We observe a clear ballistic range ($\sim t^2$) that extends up to $\tilde{t} \sim 10^{-1}$, followed by a gradual approach to diffusive scaling ($\sim t$), suggesting that the line kinematics dominate the dispersion scaling. Upon further inspection, this transition timescale of ballistic-to-diffusive scaling coincides with the walking timescale τ_m. The vertical dispersion plateaus around $\tilde{t} \sim 3$, as the dispersion distance approaches the size (height) of the room. The variations caused by buoyancy are still evident when the MSDs are plotted on a linear scale (see insets). Ambient temperature has opposing effects on horizontal and vertical dispersion of particles (see top and bottom insets)—whereas a higher ambient temperature increases vertical dispersion, it suppresses horizontal dispersion. This can be rationalized by returning to the Lagrangian trajectories of the particles shown in Fig. 5 (A and B). In the absence of buoyancy, the particles are pulled downward by the underlying downwash current while also being carried forward (horizontally) by the mean drift around the walkers. However, when the ambient temperature is increased, the horizontal dispersion is suppressed due to the lifting of plumes above the height of the currents created by the walkers. We note that the particle transport discussed here is for small aerosolized droplets (≤10 μm), where the droplet Stokes number and Froude number are sufficiently small that we can safely ignore gravitational settling and inertial clustering of the particles (*50*, *51*) for the timescales of interest. Moreover, during regular breathing of individuals in the line, the fraction of large droplets is relatively low, unlike the case of violent respiratory expulsions such as a sneeze or a cough (*5*, *57*).

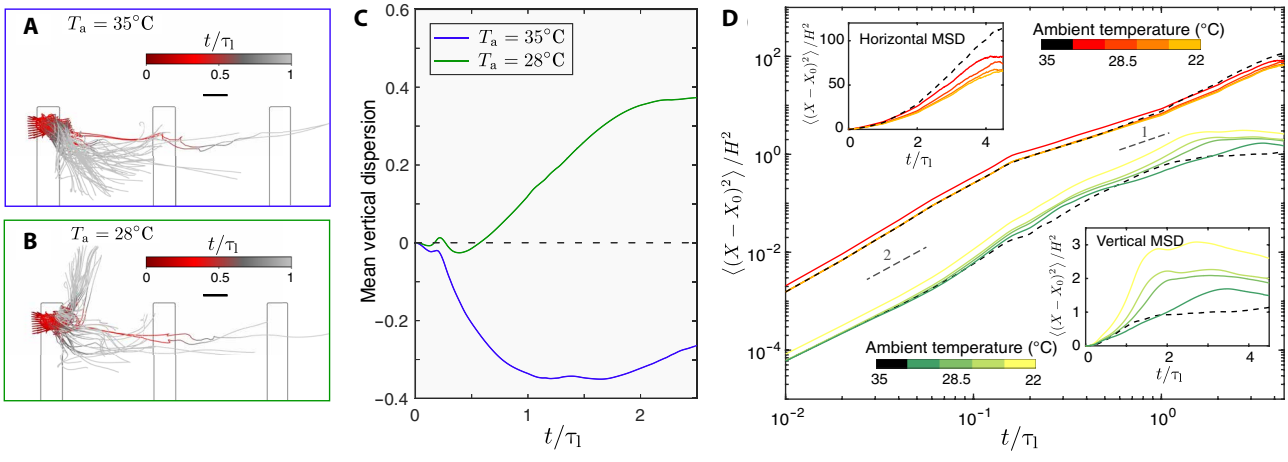

Fig. 5. Lagrangian trajectories and dispersion of particles, obtained from DNS. Plot (**A**) and (**B**) correspond to the nonbuoyant case and the buoyant case, respectively, with the particles released from the sides of the cylinder, during one period after release. The colors red to gray represent the time after release. The mean vertical dispersion of tracers is shown for the nonbuoyant (blue) and buoyant (green) cases is shown in (**C**). MSD of the Lagrangian tracer particles released from the sides of the cylinders for different net buoyancy conditions are summarized in (**D**). The upper curves are the horizontal MSD, and the lower lines are the vertical MSD of the tracers on a log-log scale. Insets show the same on data on a linear scale.

We have also examined the effect of the human body thermal plume on the transport. In particular, the strength of the body thermal plume current is low (*58*–*61*) compared to the kinematically induced air currents such as the "downwash," and the human body thermal plume is restricted to a small distance (~1 cm) from the skin surface (*62*, *63*). Although the overhead region of the cylinders is significantly modified by the body thermal plume (*62*, *63*), the body plume itself does not significantly affect the transport of the breath plume as the latter is released below head height [see also the Supplementary Materials showing DNS]. The downwash current persists, and the flow and transport within the region between the cylinders are similar even for the conditions with a large temperature gradient.

This study has provided a glimpse into the complex flow patterns created by periodic start-stop motions mimicking the kinematics of everyday interactions in waiting lines around us, from a grocery store or cafe to airports or a voting center. We have revealed the existence of fluid dynamical counter-currents that arise from the competing roles of shear (walking) and buoyancy (thermal gradients between the breath plume and ambient) in a traditional waiting line, by using a combination of laboratory experiments and DNS. The large-scale transport patterns were found to be comparable for human-shaped models and for idealized, cylindrical models having the same equivalent diameter. These counter-currents can cause significant variations in the infection risks for individuals waiting in the line. While faster-moving waiting lines strengthen the downward current (downwash), a low ambient temperature increases the buoyancy-induced upward draft of the breath plume. The ratio of the walking speed, U_m, of individuals to the free-fall velocity scale, U_b, of the breath plume determines the conditions of elevated risks. This is set up when the breath plume is very effectively counteracted by the wake downwash, causing the aerosols to linger in the air at an infectious height and at minimal dilution levels for extended time (Fig. 4B). Depending on the walking speed of individuals in the line, infection risks may be heightened at intermediate ambient temperatures (22° to 30°C), which fall within the human comfort range (*64*). However, the risks may be reduced in both hotter (≥32°C) and colder (≤22°C) ambients, which can have important implications across climatic zones (tropical to temperate climate biomes).

The findings presented here highlight the stark contrast to the transmission mechanisms in static social interactions, where flows generated by the kinematics of individuals are absent. We modeled the breath plume dynamics under the combined influence of the downwash and the thermal gradient and obtain an expression for the vertical position of the breath plume after one walking/waiting cycle as $Y - Y_0 = \left(\kappa\sqrt{\beta\Delta T} - \gamma\ U_m\right)\tau_1$. The Lagrangian statistics of the dispersion of particles show that the horizontal dispersion (MSD_h) is enhanced (suppressed) at lower (higher) ambient temperatures, while for the vertical MSD, the temperature dependence is reversed.

Additional influences from human body thermal plume were noticeable in the overhead regions of the walkers. However, the transport of the breath plume aerosols was not significantly modified by the presence of the body thermal plume due to its minimal spatial overlap with the body thermal plume (*62*, *63*). In the present work, effects of radiation heat transport were not considered. Since the body temperature is moderate, thermal radiation effects are expected to be less prominent (*40*, *58*, *62*) compared to the effects of the kinematic (downwash) and thermal currents. The conclusions drawn in the present study rely on the average walking speed and the discontinuous motion in the line, which are crucial in creating the periodic downwash current. Since the walking speed, ambient temperature, and the wait-walk time period ratio are all variables, the problem in itself presents a rich complexity in outcomes, which might account for some of the variability in infection patterns recorded in literature (*32*, *65*).

It is to be recognized that the full scope of cross-infection risks in a waiting line is truly multivariate, with biological (*66*, *67*), environmental, and behavioral factors (*65*, *68*–*71*). The present work has addressed the specific effects of line kinematics and temperature in a simplified waiting line setting, assuming a poorly ventilated indoor space. Variations in ventilation, humidity, and airflow conditions can affect the fluid dynamics of the transport and have an influence on the risks of transmission (*17*, *72*, *73*). However, indoor waiting lines with poor ventilation and moderate to high indoor temperatures are common in many developing countries, especially in tropical and equatorial regions of South Asia, sub-Saharan Africa, and Central America (*74*–*77*). Our observations indicate that even in a poorly ventilated settings, if the temperature is maintained "above a certain range" or "below a range," the risk may be lowered as the breath plume would be either driven downward or upward and prevented from lingering at head height, which might suggest a plausible mitigation strategy. There are, to be sure, uncertainties in our analysis approaches, and these insights should not be extended to the case of continuously moving (walking or running) lines, i.e., a reduced frequency $f^* \equiv \tau_m / \tau_l \to 1$, in which case the shear-driven circulation is expected to take a different form from what we report here. This is outside the scope of the present work. Future efforts at mitigation could be targeted at new, modified line arrangements where individuals are not positioned behind each other or by designing lines in which either of the two identified counter-currents is selectively suppressed, allowing for aerosols to be either pulled up or pushed down. Ventilation approaches specifically aimed for the removal of plumes could also be effective measures to reduce the cross-infection risks in waiting lines.

MATERIALS AND METHODS

The experimental setup made use of an Arduino microcontroller and a stepper motor controller to mimic the periodic movements in waiting line with precise control over walking and waiting cycles. The measurement section was located at the center of a 1.8 m–by–0.46 m–by–0.46 m water tank with a 80/20 aluminum framing. The conveyor belt was attached to two 3D printed pulleys and was driven by the stepper motor, which connected to the pulley to mimic the periodic motion of the waiting. A high-torque (12 Nm) Nema-34 stepper motor drove the periodic motion of the system via the Arduino microcontroller along with DM556 stepper motor driver. The program was coded in Arduino Integrated Development Environment, and AccelStepper library is used in the program. We mounted the system on a Teflon-coated, double-U channel system to minimize vibrations of the belt in an accelerating-decelerating system while simultaneously visualizing passive scalar transport and tracking the fluid motion. The 3D printed cylindrical dummies are glued to the conveyor belt to mimic people walking and waiting in a line (or queue). 3D printing was used to print dummies of a cylindrical shape whose diameter will be determined by matching the nondimensional parameter A^* of an actual

waiting line. Further, ensuring dynamic similarity, we designed the dummies to be around 2.5 cm in diameter and 11 cm in height for water as the working fluid. Two Photron Nova S-9 high speed cameras were used in the imaging experiments, one for the side view and the other one for the top view images for dye visualization and PIV.

The simulations were conducted on a 256–by–1024–by–512 grid, on domain sizes of $9.3D_c$ in the walking direction (horizontal), $5.3D_c$ in the transverse direction (horizontal), and $8.8D_c$ in the vertical direction, which accommodate three cylinders between the periodic domains. The domain size was determined to be sufficiently large that further increase in domain extent did not change the flow patterns significantly. The grid size was set to be uniform in the horizontal and vertical directions, with a clustered arrangement near the boundaries of the cylinders and walls. The average cell size was $0.02D_c$ in the horizontal direction and ranges between $0.015D_c$ and $0.03D_c$ in the vertical direction. Time-stepping was performed with a fractional time step method using a Courant number of 1.4, which was below the stability limit of $\sqrt{3}$. Grid convergence tests were performed to ensure that the numerical dissipation of energy was less than 1%, which in the past has been a good indicator for the convergence of the numerical method.

Supplementary Materials

The PDF file includes:
Supplementary Text
Figs. S1 to S10
Legends for movies S1 to S4

Other Supplementary Material for this manuscript includes the following:
Movies S1 to S4

REFERENCES AND NOTES

1. L. Bourouiba, The fluid dynamics of disease transmission. *Annu. Rev. Fluid Mech.* **53**, 473 (2021).
2. M. Abkarian, S. Mendez, N. Xue, F. Yang, H. A. Stone, Speech can produce jet-like transport relevant to asymptomatic spreading of virus. *Proc. Natl. Acad. Sci. U.S.A.* **117**, 25237 (2020).
3. M. L. Pöhlker, O. O. Krüger, J.-D. Förster, T. Berkemeier, W. Elbert, J. Fröhlich-Nowoisky, U. Pöschl, C. Pöhlker, G. Bagheri, E. Bodenschatz, J. A. Huffman, S. Scheithauer, E. Mikhailov, Respiratory aerosols and droplets in the transmission of infectious diseases. arXiv:2103.01188 [physics.med-ph] (2021).
4. K. L. Chong, C. S. Ng, N. Hori, R. Yang, R. Verzicco, D. Lohse, Extended lifetime of respiratory droplets in a turbulent vapor puff and its implications on airborne disease transmission. *Phys. Rev. Lett.* **126**, 034502 (2021).
5. L. Bourouiba, Turbulent gas clouds and respiratory pathogen emissions: Potential implications for reducing transmission of COVID-19. *JAMA* **323**, 1837 (2020).
6. R. Mittal, K. Breuer, J. H. Seo, The flow physics of face masks. *Annu. Rev. Fluid Mech.* **55**, 193–211 (2023).
7. J. Tang, C. Noakes, P. Nielsen, I. Eames, A. Nicolle, Y. Li, G. Settles, Observing and quantifying airflows in the infection control of aerosol-and airborne-transmitted diseases: An overview of approaches. *J. Hosp. Infec.* **77**, 213 (2011).
8. A. C. K. Lai, C. K. M. Poon, A. C. T. Cheung, Effectiveness of facemasks to reduce exposure hazards for airborne infections among general populations. *J. R. Soc. Interface* **9**, 938 (2012).
9. T. Greenhalgh, M. B. Schmid, T. Czypionka, D. Bassler, L. Gruer, Face masks for the public during the covid-19 crisis. *BMJ* **369**, m1435 (2020).
10. N. H. L. Leung, D. K. W. Chu, E. Y. C. Shiu, K.-H. Chan, J. J. McDevitt, B. J. P. Hau, H.-L. Yen, Y. Li, D. K. M. Ip, J. S. M. Peiris, W.-H. Seto, G. M. Leung, D. K. Milton, B. J. Cowling, Respiratory virus shedding in exhaled breath and efficacy of face masks. *Nat. Med.* **26**, 676–680 (2020).
11. S.-A. Lee, S. A. Grinshpun, T. Reponen, Respiratory performance offered by N95 respirators and surgical masks: Human subject evaluation with NaCl aerosol representing bacterial and viral particle size range. *Ann. Occup. Hyg.* **52**, 177 (2008).
12. R. Povaiah, Social Distancing in cabs: Why plastic panels won't be effective. *Quint* **1**, 9 (2020).
13. L. Morawska, J. W. Tang, W. Bahnfleth, P. M. Bluyssen, A. Boerstra, G. Buonanno, J. Cao, S. Dancer, A. Floto, F. Franchimon, C. Haworth, J. Hogeling, C. Isaxon, J. L. Jimenez, J. Kurnitski, Y. Li, M. Loomans, G. Marks, L. C. Marr, L. Mazzarella, M. Yao, How can airborne transmission of COVID-19 indoors be minimised? *Environ. Int.* **142**, 105832 (2020).
14. R. Zhang, Y. Li, A. L. Zhang, Y. Wang, M. J. Molina, Identifying airborne transmission as the dominant route for the spread of COVID-19. *Proc. Natl. Acad. Sci. U.S.A.* **117**, 14857 (2020).
15. I. T. Yu, Y. Li, T. W. Wong, W. Tam, A. T. Chan, J. H. Lee, D. Y. Leung, T. Ho, Evidence of airborne transmission of the severe acute respiratory syndrome virus. *N. Engl. J. Med.* **350**, 1731 (2004).
16. M. Abkarian, H. A. Stone, Stretching and break-up of saliva filaments during speech: A route for pathogen aerosolization and its potential mitigation. *Phys. Rev. Fluids* **5**, 102301 (2020).
17. R. He, W. Liu, J. Elson, R. Vogt, C. Maranville, J. Hong, Airborne transmission of COVID-19 and mitigation using box fan air cleaners in a poorly ventilated classroom. *Phys. Fluids* **33**, 057107 (2021).
18. R. K. Bhagat, M. D. Wykes, S. B. Dalziel, P. Linden, Effects of ventilation on the indoor spread of COVID-19. *J. Fluid Mech.* **903**, F1 (2020).
19. J. K. Gupta, C.-H. Lin, Q. Chen, Characterizing exhaled airflow from breathing and talking. *Indoor Air* **20**, 31 (2010).
20. M. Meselson, Droplets and aerosols in the transmission of SARS-CoV-2. *N. Engl. J. Med.* **382**, 2063 (2020).
21. J. Yan, M. Grantham, J. Pantelic, P. J. B. De Mesquita, B. Albert, F. Liu, S. Ehrman, D. K. Milton, EMIT Consortium, Infectious virus in exhaled breath of symptomatic seasonal influenza cases from a college community. *Proc. Natl. Acad. Sci. U.S.A.* **115**, 1081 (2018).
22. R. Wölfel, V. M. Corman, W. Guggemos, M. Seilmaier, S. Zange, M. A. Müller, D. Niemeyer, T. C. Jones, P. Vollmar, C. Rothe, M. Hoelscher, T. Bleicker, S. Brünink, J. Schneider, R. Ehmann, K. Zwirglmaier, C. Drosten, C. Wendtner, Virological assessment of hospitalized patients with COVID-2019. *Nature* **581**, 465 (2020).
23. W. Yang, S. Elankumaran, L. C. Marr, Concentrations and size distributions of airborne influenza A viruses measured indoors at a health centre, a day-care centre and on aeroplanes. *J. R. Soc. Interface* **8**, 1176 (2011).
24. B. Scharfman, A. Techet, J. Bush, L. Bourouiba, Visualization of sneeze ejecta: Steps of fluid fragmentation leading to respiratory droplets. *Exp. Fluids* **57**, 24 (2016).
25. P. Bahl, C. Doolan, C. de Silva, A. A. Chughtai, L. Bourouiba, C. R. MacIntyre, Airborne or droplet precautions for health workers treating coronavirus disease 2019? *J. Infect. Dis.* **189**, 1093 (2020).
26. L. Bourouiba, E. Dehandschoewercker, J. W. Bush, Violent expiratory events: On coughing and sneezing. *J. Fluid Mech.* **745**, 537 (2014).
27. N. Van Doremalen, T. Bushmaker, D. H. Morris, M. G. Holbrook, A. Gamble, B. N. Williamson, A. Tamin, J. L. Harcourt, N. J. Thornburg, S. I. Gerber, J. O. Lloyd-Smith, E. de Wit, V. J. Munster, Aerosol and surface stability of SARS-CoV-2 as compared with SARS-CoV-1. *N. Engl. J. Med.* **382**, 1564 (2020).
28. V. Stadnytskyi, C. E. Bax, A. Bax, P. Anfinrud, The airborne lifetime of small speech droplets and their potential importance in SARS-CoV-2 transmission. *Proc. Natl. Acad. Sci. U.S.A.* **117**, 11875 (2020).
29. V. Mathai, A. Das, K. Breuer, Aerosol transmission in passenger car cabins: Effects of ventilation configuration and driving speed. *Phys. Fluids* **34**, 021904 (2022).
30. F. Yang, A. A. Pahlavan, S. Mendez, M. Abkarian, H. A. Stone, Towards improved social distancing guidelines: Space and time dependence of virus transmission from speech-driven aerosol transport between two individuals. *Phys. Rev. Fluids* **5**, 122501 (2020).
31. C. B. Beggs, S. J. Shepherd, K. G. Kerr, Potential for airborne transmission of infection in the waiting areas of healthcare premises: Stochastic analysis using a Monte Carlo model. *BMC Infect. Dis.* **10**, 247 (2010).
32. V. Mathai, The air we breathe in a car. *Phys. Today* **74**, 66 (2021).
33. J. W. Tang, T. J. Liebner, B. A. Craven, G. S. Settles, A schlieren optical study of the human cough with and without wearing masks for aerosol infection control. *J. R. Soc. Interface* **6**, S727 (2009).
34. S. Verma, M. Dhanak, J. Frankenfield, Visualizing droplet dispersal for face shields and masks with exhalation valves. *Phys. Fluids* **32**, 091701 (2020).
35. R. Mittal, R. Ni, J.-H. Seo, The flow physics of COVID-19. *J. Fluid Mech.* **894**, 330 (2020).
36. A. Blass, P. Tabak, R. Verzicco, R. J. Stevens, D. Lohse, The effect of Prandtl number on turbulent sheared thermal convection. *J. Fluid Mech.* **910**, A37 (2021).
37. A. Blass, X. Zhu, R. Verzicco, D. Lohse, R. J. A. M. Stevens, Flow organization and heat transfer in turbulent wall sheared thermal convection. *J. Fluid Mech.* **897**, A22 (2020).
38. Y. Wang, J. Yang, Y. Chen, H. Liu, M. Gruteser, R. P. Martin, in *Proc. 12th Annu. Int. Conf. Mobile Syst.* (Association for Computing Machinery, 2014), pp. 42–54.
39. J. M. Donelan, R. Kram, Exploring dynamic similarity in human running using simulated reduced gravity. *J. Exp. Biol.* **203**, 2405–2415 (2000).
40. R. Yang, C. S. Ng, K. L. Chong, R. Verzicco, D. Lohse, Do increased flow rates in displacement ventilation always lead to better results? *J. Fluid Mech.* **932**, A3 (2022).

41. Y. Houdas, E. Ring, *Human Body Temperature: Its Measurement and Regulation* (Springer Science & Business Media, 2013).
42. E. Fadlun, R. Verzicco, P. Orlandi, J. Mohd-Yusof, Combined immersed-boundary finite-difference methods for three-dimensional complex flow simulations. *J. Comput. Phys.* **161**, 35 (2000).
43. E. P. Van Der Poel, R. Ostilla-Mónico, J. Donners, R. Verzicco, A pencil distributed finite difference code for strongly turbulent wall-bounded flows. *Comput. Fluids* **116**, 10 (2015).
44. P. L. Garcia-Ybarra, A. Pinelli, Turbulent channel flow concentration profile and wall deposition of a large Schmidt number passive scalar. *Compt. Rend. Méc.* **334**, 531–538 (2006).
45. R. McKeown, R. Ostilla-Mónico, A. Pumir, M. P. Brenner, S. M. Rubinstein, Cascade leading to the emergence of small structures in vortex ring collisions. *Phys. Rev. Fluids* **3**, 124702 (2018).
46. R. McKeown, R. Ostilla-Mónico, A. Pumir, M. P. Brenner, S. M. Rubinstein, Turbulence generation through an iterative cascade of the elliptical instability. *Sci. Adv.* **6**, eaaz2717 (2020).
47. R. K. Zeytounian, Joseph Boussinesq and his approximation: A contemporary view. *Comptes Rendus Mecanique* **331**, 575 (2003).
48. D. Pullin, A. Perry, Some flow visualization experiments on the starting vortex. *J. Fluid Mech.* **97**, 239 (1980).
49. H. Jiang, X. Zhu, V. Mathai, R. Verzicco, D. Lohse, C. Sun, Controlling heat transport and flow structures in thermal turbulence using ratchet surfaces. *Phys. Rev. Lett.* **120**, 044501 (2018).
50. V. Mathai, D. Lohse, C. Sun, Bubbly and buoyant particle–laden turbulent flows. *Annu. Rev. Condens. Matter Phys.* **11**, 529 (2020).
51. V. Mathai, E. Calzavarini, J. Brons, C. Sun, D. Lohse, Microbubbles and microparticles are not faithful tracers of turbulent acceleration. *Phys. Rev. Lett.* **117**, 024501 (2016).
52. S. Yang, G. W. Lee, C.-M. Chen, C.-C. Wu, K.-P. Yu, The size and concentration of droplets generated by coughing in human subjects. *J. Aerosol Med.* **20**, 484–494 (2007).
53. F. K. Gregson, N. A. Watson, C. M. Orton, A. E. Haddrell, L. P. McCarthy, T. J. Finnie, N. Gent, G. C. Donaldson, P. L. Shah, J. D. Calder, B. R. Bzdek, D. Costello, J. P. Reid, Comparing aerosol concentrations and particle size distributions generated by singing, speaking and breathing. *Aerosol Sci. Tech.* **55**, 681 (2021).
54. K. P. Fennelly, Particle sizes of infectious aerosols: Implications for infection control. *Lancet Respir. Med.* **8**, 914 (2020).
55. R. S. Papineni, F. S. Rosenthal, The size distribution of droplets in the exhaled breath of healthy human subjects. *J. Aerosol Med.* **10**, 105–116 (1997).
56. W. Van De Water, N. Dam, E. Calzavarini, Dispersion of molecular patterns written in turbulent air. *Phys. Rev. Lett.* **129**, 254501 (2022).
57. G. A. Somsen, C. van Rijn, S. Kooij, R. A. Bem, D. Bonn, Small droplet aerosols in poorly ventilated spaces and SARS-CoV-2 transmission. *Lancet Respir. Med.* **8**, 658 (2020).
58. B. A. Craven, G. S. Settles, A computational and experimental investigation of the human thermal plume. *J. Fluids Eng.* **128**, 1251–1258 (2006).
59. C. Wang, J. Liu, J. Li, F. Li, Chaotic behavior of human thermal plumes in an aircraft cabin mockup. *Int. J. Heat Mass Transf.* **119**, 223 (2018).
60. M. Salmanzadeh, G. Zahedi, G. Ahmadi, D. Marr, M. Glauser, Computational modeling of effects of thermal plume adjacent to the body on the indoor airflow and particle transport. *J. Aerosol Sci.* **53**, 29 (2012).
61. A. Bogdan, K. Ogłodziński, M. Szyłak-Szydłowski, Analysis of thermal plumes forming over male human subjects. *J. Building Eng.* **45**, 103596 (2022).
62. Y. Liu, Y. Zhao, Z. Liu, J. Luo, in *Building Simulation* (Springer, 2016), vol. 9, pp. 677–687.
63. A. W. Gena, C. Voelker, G. S. Settles, Qualitative and quantitative schlieren optical measurement of the human thermal plume. *Indoor Air* **30**, 757 (2020).
64. F. Nicol, H. B. Rijal, H. Imagawa, R. Thapa, The range and shape of thermal comfort and resilience. *Energ. Buildings* **224**, 110277 (2020).
65. L. Morawska, G. Buonanno, The physics of particle formation and deposition during breathing. *Nat. Rev. Phys.* **3**, 300 (2021).
66. G. Benchetrit, Breathing pattern in humans: Diversity and individuality. *Respir. Physiol.* **122**, 123–129 (2000).
67. M. Tobin, Breathing pattern analysis. *Intensive Care Med.* **18**, 193–201 (1992).
68. J. J. Kavanagh, H. B. Menz, Accelerometry: A technique for quantifying movement patterns during walking. *Gait Posture* **28**, 1 (2008).
69. N. Sekiya, H. Nagasaki, Reproducibility of the walking patterns of normal young adults: Test-retest reliability of the walk ratio(step-length/step-rate). *Gait Posture* **7**, 225–227 (1998).
70. M. P. Murray, A. B. Drought, R. C. Kory, Walking patterns of normal men. *JBJS* **46**, 335 (1964).
71. M. P. Murray, R. C. Kory, B. H. Clarkson, S. Sepic, Comparison of free and fast speed walking patterns of normal men. *Am. J. Phys. Med. Rehabil.* **45**, 8 (1966).
72. Y. Li, P. Cheng, W. Jia, Poor ventilation worsens short-range airborne transmission of respiratory infection. *Indoor Air* **32**, e12946 (2022).
73. Y. Lu, Y. Li, H. Zhou, J. Lin, Z. Zheng, H. Xu, B. Lin, M. Lin, L. Liu, Affordable measures to monitor and alarm nosocomial SARS-CoV-2 infection due to poor ventilation. *Indoor Air* **31**, 1833 (2021).
74. S. Ehsan, F. Abbas, M. Ibrahim, B. Ahmad, A. A. Farooque, Thermal discomfort levels, building design concepts, and some heat mitigation strategies in low-income communities of a South Asian city. *Int. J. Environ. Res. Public Health* **18**, 2535 (2021).
75. P. Tasgaonkar, D. Zade, S. Ehsan, G. Gorti, N. Mamnun, C. Siderius, T. Singh, Indoor heat measurement data from low-income households in rural and urban South Asia. *Sci. Data* **9**, 285 (2022).
76. M. U. Adaji, T. O. Adekunle, R. Watkins, G. Adler, Indoor comfort and adaptation in low-income and middle-income residential buildings in a Nigerian city during a dry season. *Build. Environ.* **162**, 106276 (2019).
77. F. Pavanello, E. De Cian, M. Davide, M. Mistry, T. Cruz, P. Bezerra, D. Jagu, S. Renner, R. Schaeffer, A. F. Lucena, Air-conditioning and the adaptation cooling deficit in emerging economies. *Nat. Commun.* **12**, 6460 (2021).

Acknowledgments: We thank the reviewers for useful comments. We thank Y. Zhu and A. Pandey for useful insights into the experiments and numerical simulations. V.M. acknowledges useful discussions with D. Lohse and X. Zhu. **Funding:** We acknowledge support from the UMass faculty startup fund, the Commonwealth Honors College, the UMass SOAR Fund, and the Emergia Program of the Junta de Andalucía (Spain). **Author contributions:** V.M. conceived the research. R.L. and V.M. designed the experiments. R.L. and M.V.M. performed the experiments. R.O.M. and G.A.T. wrote the software, carried out the numerical simulations, and curated the data. R.L. analyzed the experimental and numerical data, and M.V.M. conducted additional analyses of human-shaped models. All authors discussed the results and contributed to the writing. **Competing interests:** The authors declare that they have no competing interests. **Data and materials availability:** All data needed to evaluate the conclusions in the paper are present in the paper and/or the Supplementary Materials.

Submitted 4 February 2025
Accepted 3 July 2025
Published 6 August 2025
10.1126/sciadv.adw0985